
M2NO: Multiresolution Operator Learning with Multiwavelet-based Algebraic Multigrid Method

Zhihao Li

The Hong Kong University
of Science and Technology (Guangzhou)
zli416@connect.hkust-gz.edu.cn

Zhilu Lai

The Hong Kong University
of Science and Technology (Guangzhou)
zhilulai@ust.hk

Xiaobo Zhang

Southwest Jiaotong University
zhangxb@swjtu.edu.cn

Wei Wang*

The Hong Kong University
of Science and Technology (Guangzhou)
weiwcs@ust.hk

Abstract

Solving partial differential equations (PDEs) effectively necessitates a multi-scale approach, particularly critical in high-dimensional scenarios characterized by increasing grid points or resolution. Traditional methods often fail to capture the detailed features necessary for accurate modeling, presenting a significant challenge in scientific computing. In response, we introduce the Multiwavelet-based Algebraic Multigrid Neural Operator (M2NO), a novel deep learning framework that synergistically combines multiwavelet transformations and algebraic multigrid (AMG) techniques. By exploiting the inherent similarities between these two approaches, M2NO overcomes their individual limitations and enhances precision and flexibility across various PDE benchmarks. Employing Multiresolution Analysis (MRA) with high-pass and low-pass filters, the model executes hierarchical decomposition to accurately delineate both global trends and localized details within PDE solutions, supporting adaptive data representation at multiple scales. M2NO also automates node selection and adeptly manages complex boundary conditions through its multiwavelet-based operators. Extensive evaluations on a diverse array of PDE datasets with different boundary conditions confirm M2NO's superior performance. Furthermore, M2NO excels in handling high-resolution and super-resolution tasks, consistently outperforming competing models and demonstrating robust adaptability in complex computational scenarios.

1 Introduction

Partial differential equations (PDEs) are fundamental to modeling a wide range of phenomena across science and engineering [13], including fluid dynamics [28, 24], material stress analysis [32], and atmospheric conditions. Traditionally, solving these equations requires specific numerical methods, designed to address individual problem characteristics, often resulting in significant computational efforts [17]. Recent developments in deep learning have introduced alternative approaches to solving PDEs [25, 22, 23, 8, 21], featuring methods like Fourier Neural Operators (FNO) [22], Galerkin Transformers (GT) [8] and Deep Operator Networks (DeepONet)[23]. These techniques leverage neural network architectures to approximate the mappings between parameters and solutions in infinite-dimensional spaces, efficiently addressing both forward and inverse problems in PDEs.

*Corresponding author

Among these techniques, the Fourier Neural Operators (FNO) [22, 20] stand out as a particularly significant development. FNO integrates Fast Fourier Transforms within a neural network framework, effectively learning direct mappings between infinite-dimensional function spaces. This capability marks FNO as a powerful tool, offering a scalable and efficient alternative to traditional numerical methods for solving PDEs.

A primary limitation of the Fourier Neural Operator (FNO) is its reliance on basis functions generated by Fast Fourier Transforms (FFTs). These functions are localized in frequency but lack spatial resolution, leading to difficulties in managing complex boundary conditions and capturing local features in high-dimensional PDEs [2, 9]. In contrast, wavelets provide both spatial and frequency localization [9, 2, 3], which enhances the management of discontinuities and improves image pattern recognition over FFTs. Despite these advantages, the Multiwavelet Transformation (MWT) model, which utilizes wavelet kernels computed by four independent neural networks, faces its own set of challenges. While leveraging Multi-Resolution Analysis (MRA) to provide a detailed representation of both frequency and spatial information, MWT requires substantial computational resources during training and struggles with grid sizes that are not powers of two, which limits its generalizability and practical application [12].

This limitation in MWT serves as a segue into discussing the Algebraic Multigrid (AMG) method. Although AMG is highly effective in improving computational efficiency in numerical computing, it is traditionally constrained by its compatibility with only simple periodic boundary conditions. Moreover, AMG requires the pre-determination of mapping operators between grid points at each level, which poses further limitations on its generalizability and practicality [6, 35, 29, 4].

In response to these limitations, we introduce an innovative neural network architecture, the Multiwavelet-based Algebraic Multigrid Neural Operator (M2NO), which synergistically combines the strengths of algebraic multigrid methods and multiresolution analysis [5, 11, 7]. Our contributions are designed to overcome the specific challenges faced by previous models:

- **Enhanced Operator Learning:** M2NO merges algebraic multigrid and multiresolution techniques to facilitate adaptive learning across multiple resolutions. This integration not only enables automatic node selection but also significantly improves the handling of complex PDE coefficients and intricate boundary conditions.
- **Advanced Operator Design:** We develop advanced prolongation and restriction operators based on multiwavelet theory. These operators are critical components of our neural operator framework, enabling efficient hierarchical decomposition that captures both global and local structural details within PDE solutions.
- **Empirical Validation:** M2NO is rigorously tested across a variety of 1D and 2D PDE datasets under different boundary conditions. Our experiments confirm its superior accuracy and scalability, consistently outperforming traditional models at various resolution scales.

These innovations underscore our commitment to advancing PDE computational frameworks, offering robust solutions for complex mathematical challenges in scientific computing.

2 Algebraic Multigrid Method and Multiwavelet

In this section, we first provide a concise overview of the algebraic multigrid method [35, 6] and multiresolution analysis using multiwavelets [1, 9]. We then summarize the similarities between these approaches and illustrate how they inform our development of multiwavelet-based prolongation and restriction operators.

2.1 Algebraic Multigrid Method

The algebraic multigrid method is a well-grounded numerical technique for solving systems of algebraic equations that approximate partial differential equations (PDEs). Specifically, we address the problem of solving the linear equation system:

$$A^h u^h = b^h, \tag{1}$$

where A^h and b^h are derived from the discretization of a differential equation on a grid Ω^h , with h representing the step size.

Given a prolongation operator, I_{2h}^h , where the superscript denotes the fine grid and the subscript denotes the coarse grid, alongside a restriction operator, I_h^{2h} , we can recursively define a multigrid method. In the two-level V-cycle method, we first perform a few relaxation steps (typically one or two) on the fine grid Ω^h to obtain an initial estimate u^h . Subsequently, we calculate the residual $r^h = b^h - A^h u^h$; restrict this residual to the coarse grid Ω^{2h} , yielding Ω^{2h} , $r^{2h} = I_h^{2h} r^h$; and solve the error equation

$$A^{2h} e^{2h} = r^{2h} \quad (2)$$

on the coarse grid. After solving, update the solution on the fine grid by setting

$$u^h = u^h + I_{2h}^h e^{2h} \quad (3)$$

and perform another few relaxation steps (typically one or two) on the fine grid. This procedure outlines the foundational steps of the V-cycle multigrid scheme, which is recursively defined, as shown in Algorithm 1. For a comprehensive discussion and theoretical grounding of the Algebraic Multigrid (AMG) methods, please refer to the Appendix A.

2.2 Multiwavelets

Wavelets are powerful tools for decomposing data, functions, or operators into different frequency components and analyzing them through scaling. They can form a complete orthonormal basis for $L^2(\mathbb{R})$. Due to their scaling properties, wavelet functions have time or space widths inversely related to their frequencies: they are narrow at high frequencies and broad at low frequencies. This characteristic ensures excellent localization in both the frequency domain and physical space, making wavelets particularly effective for analyzing phenomena across multiple scales.

A multiresolution analysis (MRA) using multiwavelets involves a sequence of closed subspaces, defined as:

$$\mathbf{V}_0^k \subset \mathbf{V}_1^k \subset \dots \subset \mathbf{V}_n^k \subset \dots$$

For $k = 1, 2, \dots$, and $n = 0, 1, 2, \dots$, we define \mathbf{V}_n^k as a space of piecewise polynomial functions with dimension $2^n k$, that satisfy certain conditions. The multiwavelet subspace \mathbf{W}_n^k , defined as the orthogonal complement of \mathbf{V}_n^k in \mathbf{V}_{n+1}^k , satisfies:

$$\mathbf{V}_n^k \oplus \mathbf{W}_n^k = \mathbf{V}_{n+1}^k, \quad \mathbf{W}_n^k \perp \mathbf{V}_n^k, \quad (4)$$

and the dimension of \mathbf{W}_n^k is of dimension $2^n k$. Therefore, the composition of spaces is:

$$\mathbf{V}_n^k = \mathbf{V}_0^k \oplus \mathbf{W}_0^k \oplus \mathbf{W}_1^k \oplus \dots \oplus \mathbf{W}_{n-1}^k. \quad (5)$$

The operators H and G , which transform the basis of the space V_j (for $j \in \mathbb{Z}^+$) to the bases of the spaces V_{j-1} and W_{j-1} respectively, exhibit the following properties (assuming H and G are real-valued):

$$\begin{aligned} H^T H + G^T G &= I \\ H G^T &= G H^T = 0 \\ H H^T &= G G^T = I. \end{aligned}$$

In the two-dimensional discrete wavelet transform, depicted in Fig 4(a), H and G function as low-pass and high-pass filters, respectively, allowing the partitioning of frequency components at each level. Fi 4(b) visually represents this decomposition in a matrix format, enhancing our understanding of how submatrices B_n , C_n , and D_n are derived from L_n .

The wavelet transform is defined as $\mathcal{W} : V_j \rightarrow V_{j-1} \oplus W_{j-1}$ (for $j \in \mathbb{Z}^+$), and given by:

$$\mathcal{W} = \begin{pmatrix} H \\ G \end{pmatrix} \quad (6)$$

Owing to the orthogonality properties of H and G , \mathcal{W} maintains orthogonality. For detailed definitions of H , G , and \mathcal{W} in 1D and 2D contexts, please refer to Appendix B.

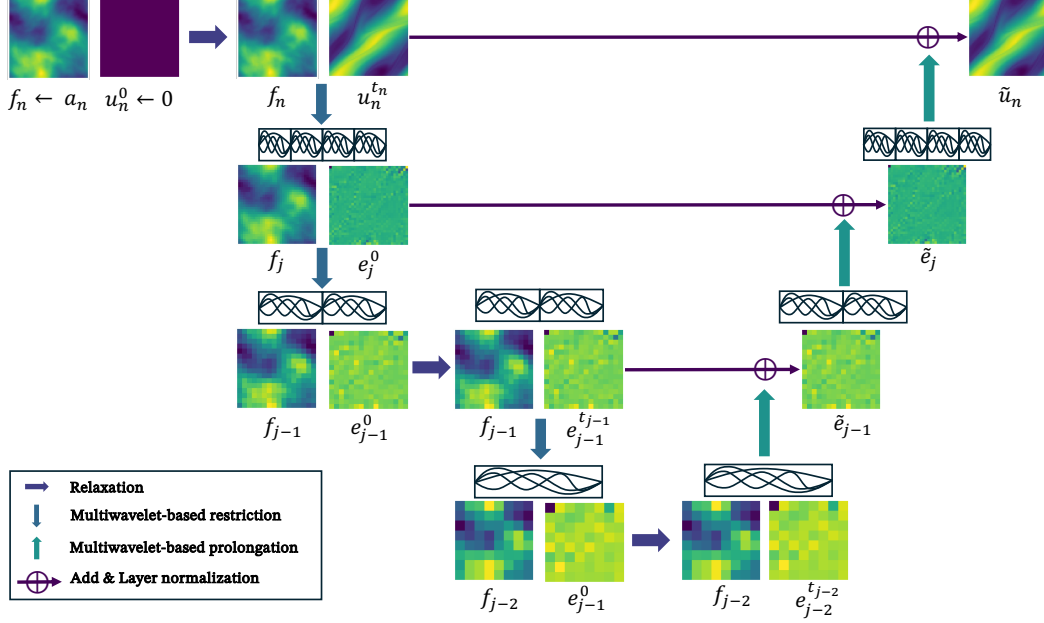


Figure 1: **Illustration of the multiwavelet-based multigrid method for PDEs.** The diagram outlines the method’s workflow, starting with the initial function f_n and guess u_n^0 . It includes pre-smoothing, multiwavelet-based restriction, solution of correction equations, prolongation back to finer grids, and post-smoothing, illustrating the data flow and transformations within the multigrid process.

2.3 Similarities between algebraic multigrid and multiresolution

Our objective in comparing these two methodologies is to explore how each enhances the other, as detailed in the following points:

1. The highest resolution space V_n in Multiresolution Analysis (MRA) aligns with Ω^h , which represents the space of the finest grid vectors in the multigrid method.
2. The decomposition step in MRA, where data is broken down, corresponds to the restriction operation in multigrid methods. Similarly, the forward wavelet transform aligns with the restriction operator I_h^{2h} .
3. The reconstruction step in MRA, which reassembles the data, is equivalent to the prolongation operation in multigrid methods. Correspondingly, the inverse wavelet transform is equivalent to the prolongation operator I_{2h}^h .
4. The orthogonality condition $WW^T = I$ corresponds to the identity relationship for the grid transfer operators, $I_h^{2h} I_{2h}^h = I$.
5. The multiresolution structure $V_n = V_{n-1} \oplus W_{n-1}$ in MRA parallels the multigrid structure $\Omega^h = \text{Range}\{I_{2h}^h\} \oplus \text{Nullspace}\{I_h^{2h}\}$.

These comparisons highlight the synergy between the algebraic multigrid and multiresolution properties of wavelet transforms and the error smoothing and correcting capabilities of intergrid operators in multigrid methods.

3 Multiwavelet-based Algebraic Multigrid Neural Operator

Building on the synergistic qualities of algebraic multigrid and multiresolution wavelet transforms discussed previously, this section elaborates on the Multiwavelet-based Multigrid Neural Operator (M2NO). We begin by defining the problem and its theoretical basis in section 3.1, then detail the construction and practical implementation of multiwavelet-based operators in section 3.2, and finally, illustrate the diverse applications of these methodologies in solving discrete PDEs in section 3.3.

3.1 Problem definition

Formally, let \mathcal{A} and \mathcal{U} denote two Sobolev spaces $\mathcal{H}^{s,p}$ with $s > 0$ and $p \geq 1$. In this context, the operator T maps from \mathcal{A} to \mathcal{U} , $T : \mathcal{A} \rightarrow \mathcal{U}$. We focus on cases where $s > 0$ and $p = 2$, choosing $p = 2$ specifically to enable the definition of projections within a Hilbert space structure, using measures μ .

We define the operator T as an integral operator with a kernel K , where $K : D \times D \rightarrow L^2$. The action of T on an element $a \in \mathcal{A}$ is given by the integral equation:

$$Ta(x) = \int_D K(x,y)a(y)dy. \quad (7)$$

This setup allows T to operate within the framework of Hilbert spaces, leveraging the properties of L^2 spaces to facilitate analysis and computations involving the operator.

An illustrative application of the theory described is the learning of the solution operator for a parametric partial differential equation (PDE). Let \mathcal{L}_a denote a differential operator that varies with a parameter $a \in \mathcal{A}$. Consider the general PDE defined as:

$$(\mathcal{L}_a u)(x) = f(x), \quad x \in D, \quad (8)$$

where D is a bounded, open subset of \mathbb{R}^d , f is a function residing in an appropriate function space, and the equation is subject to a boundary condition on ∂D . Assuming the PDE is well-posed, which implies there exists a unique solution under reasonable assumptions on the data and parameters, we define the operator $F^\dagger : \mathcal{A} \rightarrow \mathcal{U}$. This operator maps the parameter a to the solution u of (8), effectively encapsulating the dependency of the solution on the parameter within a functional mapping framework.

3.2 Multiwavelet-based Restriction and Prolongation Operators

Given an orthonormal polynomial (OP) basis for V_0^k as $\{\phi_0, \phi_1, \dots, \phi_{k-1}\}$ with respect to the measure μ_0 , we can generate the basis for subsequent spaces V_n^k for $n > 1$ through shift and scale (hence the multi-scale aspect) operations on the original basis:

$$\phi_{jl}^n = 2^{\frac{n}{2}} \phi_j(2^n x - l), \quad j = 0, \dots, k-1, \quad l = 0, \dots, 2^n - 1, \quad \text{w.r.t. } \mu_n, \quad (9)$$

where μ_n is derived from the shift and scale transformations of μ_0 . The filter coefficients construct the scaling function ϕ and wavelet ψ ; in our context, functions ϕ and ψ are known, and we utilize them to determine the filter coefficients $(H^{(0)}, H^{(1)}, G^{(0)}, G^{(1)})$, as they transform from a fine scale $n = 1$ to a coarser scale $n = 0$. A uniform measure μ_0 version is discussed in [1], and [12] extends it to arbitrary measures by incorporating correction terms $\sum^{(0)}$ and $\sum^{(1)}$.

In one dimension, the operators H and G are constructed as

$$H = \begin{pmatrix} H^{(0)} & H^{(1)} \end{pmatrix}, \quad G = \begin{pmatrix} G^{(0)} & G^{(1)} \end{pmatrix}, \quad (10)$$

to transform the basis of space V_j to the bases of spaces V_{j+1} and W_{j+1} , respectively. In two dimensions, we utilize the tensor product of one-dimensional multiresolution analyses:

$$H = H_y \otimes H_x, \quad G = \begin{pmatrix} G_y \otimes H_x \\ H_y \otimes G_x \\ G_y \otimes G_x \end{pmatrix}, \quad (11)$$

where \otimes denotes the Kronecker product. For detailed explanation, see Appendix B.

3.2.1 Low-Pass Filter based Operator

One intuitive way is using the low-pass filter as a restriction operator for the multigrid. The restriction operator and prolongation operator is define as

$$I_h^{2h} = H, \quad I_{2h}^h = (I_h^{2h})^T = H^T. \quad (12)$$

At each decomposition level, it is predominantly the low-pass filters that encapsulate the approximation of the original matrix as illustrated in each one of the levels of scale in Fig 4. In the majority of

cases, this methodology proves functional because the residual error associated with the matrices B , C , and D is almost negligible. However, this property is not maintained by the multigrid method in certain complex scenarios, such as those involving oscillatory coefficients.

Parametrization. With the explicit computation of the low-pass filter H , we take the LPF restriction operator as $I_h^{2h} = H$ and the corresponding LPF prolongation operator as $I_{2h}^h = H^T$. It is noteworthy that the prolongation operator is identical for both spaces V_0 and V_1 , which correspond to the coarsest and the next finer grids, respectively.

3.2.2 Schur complement based Operator

To circumvent these limitations, we introduce a novel set of restriction and prolongation operators, which are founded upon wavelet transformation and the Schur complement. Applying the wavelet transform to both sides of the equation and using the orthogonality of \mathcal{W} , we obtain

$$(\mathcal{W}\mathcal{L}_j\mathcal{W}^T)\mathcal{W}u = \mathcal{W}f. \quad (13)$$

Denote $\tilde{\mathcal{L}}_j = \mathcal{W}\mathcal{L}_j\mathcal{W}^T$, which is partitioned as

$$\tilde{\mathcal{L}}_j = \begin{pmatrix} T_j & B_j \\ C_j & D_j \end{pmatrix}. \quad (14)$$

Using the block UDL decomposition of $\tilde{\mathcal{L}}_j$ and the Schur complement [11, 10], the inverse $\tilde{\mathcal{L}}_j^{-1}$ is expressed as

$$u = \begin{pmatrix} H^T - G^T D_j^{-1} C_j & G^T \end{pmatrix} \begin{pmatrix} (T_j - B_j D_j^{-1} C_j)^{-1} & 0 \\ 0 & D_j^{-1} \end{pmatrix} \begin{pmatrix} H - B_j D_j^{-1} G \\ G \end{pmatrix} f. \quad (15)$$

The restriction and prolongation operator is defined as

$$I_{2h}^h = \sqrt{2}(H^T - G^T D_j^{-1} C_j), \quad I_h^{2h} = \frac{1}{\sqrt{2}}(H - B_j D_j^{-1} G). \quad (16)$$

For detailed explanations and derivations, please refer to the Appendix B.4.

Parametrization. The multiwavelet-based restriction operator and prolongation operator are approximated using three single-layered CNNs, denoted by B and C and D^{-1} , while H and G are precomputed. For a detailed implementation of the model configuration, see Appendix F.2.

3.3 Multiwavelet-based Algebraic Multigrid Method for Discrete PDEs

Employing a linear Finite Element Method (FEM) discretization with mesh size $h = \frac{1}{d}$, the discretized system is described by:

$$A_j * u_j = f_j, \quad (17)$$

where $u_j, f_j \in \mathbb{R}^{d \times d}$. In this model, $*$ denotes the convolution operation for a single channel, using a 3×3 kernel A determined by the elliptic operator and specific boundary conditions. The inverse of $A*$ aligns with the discrete Green's function in a linear FEM context. The V-cycle multigrid approach, which can be represented as a conventional convolutional neural network, effectively solves this equation [16, 14].

We provide a concise overview of the essential components of the multigrid structure as shown in Fig 1, framed in the language of convolution as an operator mapping from f to u :

1. **Initialization:** Set the initial function f_n as a_n and the initial guess $u_j^0 (j = 0, \dots, n)$.
2. **Pre-smoothing:** Apply s_n steps of the smoothing iteration S_n to obtain an approximation:

$$u_n^i = u_n^{i-1} + S_n^i * (f_n - A_n * u_n^{i-1}), \quad i = 1, \dots, s_n. \quad (18)$$

3. **Multigrid correction:** Transition to a coarser grid, where a coarse grid operator A_{j-1} (for $j = 1, \dots, n$) is defined. The residual $r_j = f_j - A_j * u_j^{s_j}$ is restricted using a multiwavelet-based restriction operator I_h^{2h} , defined in (16). The correction equation $A_{j-1} e_{j-1} = r_{j-1}$ is then solved over a few relaxation steps s_{j-1} . The result, e_{j-1} , is prolonged back to the

finer grid using the multiwavelet-based prolongation operator I_{2h}^h , as defined in (16), to update the approximation:

$$f_{j-1} = I_h^{2h}(f_j - A_j * u_j^{s_j}), \quad (19)$$

$$u_{j-1}^i = u_{j-1}^{i-1} + S_{j-1}^i * f_{j-1}, \quad i = 1, \dots, s_{j-1}, \quad (20)$$

$$\tilde{u}_j = u_j^{s_j} + I_{2h}^h u_{j-1}^{s_{j-1}}. \quad (21)$$

4. **Post-processing:** At this stage, one may choose to further prolongate to a finer level in a process known as super-resolution or continue with post-smoothing steps.

The following theorem establishes the convergence properties of the V-cycle multigrid operator. The detailed proof of this theorem is provided in the Appendix C.

Theorem 1 (Operator Convergence [34]). *Let us denote the V-cycle multigrid operator as \mathcal{L}_{mg} . The convergence can be succinctly expressed by the inequality*

$$\|u - \mathcal{L}_{mg}(A * u)\|_A \leq \left(1 - \frac{1}{c}\right) \|u\|_A, \quad (22)$$

where c represents a constant that remains unaffected by the discretization parameter h .

The above theorem affirms the uniform approximation efficacy of \mathcal{L}_{mg} in relation to the pseudo-inverse of A^* , associated with the Green's function for the elliptic operator L_n . The notation $\|u\|_A^2 = (u, A * u)_{\mathbb{L}^2(\Omega)}$ defines the energy norm within the domain Ω .

Table 1: **Performance comparison with baselines on benchmarks.** L_2 loss is recorded. For clarity, the best result is in bold and the second best is underlined. The results presented in this table were obtained at the highest resolution settings.

Model	1D		2D			
	Advection	Burgers	Darcy	Navier-Stoke		Diffusion-Reaction
	$\nu = 1e - 3$	$\beta = 4.0$		$\nu = 1e - 3$	$\nu = 1e - 5$	
UNet	3.44E-05	3.83E-05	1.54E-01	3.86E-03	2.15E-02	1.46E-01
FNO-2D	1.68E-05	1.81E-05	1.95E-02	4.95E-03	1.72E-02	1.64E-01
MGNO	/	/	5.72E-02	3.39E-03	1.27E-02	1.12E-01
MWT-Leg	9.91E-06	2.07E-05	<u>1.91E-02</u>	1.83E-03	1.19E-02	1.15E-01
LSM	/	/	6.69E-02	6.00E-03	1.71E-02	1.58E-01
M2NO	2.14E-06	7.16E-06	2.73E-02	9.17E-04	4.07E-03	1.01E-01
M2NO-LPF	<u>2.35E-06</u>	<u>7.52E-06</u>	9.64E-03	<u>1.04E-03</u>	<u>6.39E-03</u>	<u>1.06E-01</u>
Promotion	78.41%	60.49%	49.56%	49.75%	65.77%	10.15%

4 Experiments

In this section, we evaluate the performance of the M2NO model on a variety of PDE benchmarks, incorporating different boundary conditions, and conduct Multiresolution Analysis. Specifically, we focus on two variants: M2NO with a Schur complement based Operator and M2NO-LPF featuring a Low-Pass Filter based Operator. These variants are assessed to understand their respective impacts on solving complex PDEs under varied computational scenarios.

General Setting. We consider a set of function pairs $(a_i, u_i)_{i=1}^N$, where $a_i = a(x_i)$ and $u_i = u(x_i)$ at discretized points x_i in the domain D . We express the functions f_a and f_u as linear combinations of basis functions ϕ_{ji}^n , formulated as $f_a = \sum_{i=1}^N a_i \phi_{ji}^n$ and $f_u = \sum_{i=1}^N u_i \phi_{ji}^n$, both of which belong to the space V_n^k where $n = \log_2 N$. These formulations serve as notational conventions rather than explicit constructs. Given the dataset $(a_i, u_i)_{i=1}^N$, our goal is to approximate the operator \mathcal{G} by optimizing network parameters θ . This involves solving the following optimization problem:

$$\min_{\theta \in \Theta} \mathcal{L}(\theta) := \min_{\theta \in \Theta} \frac{1}{N} \sum_{i=1}^N \left[\|\tilde{\mathcal{G}}_{\theta}(a_i) - u_i\|^2 \right]. \quad (23)$$

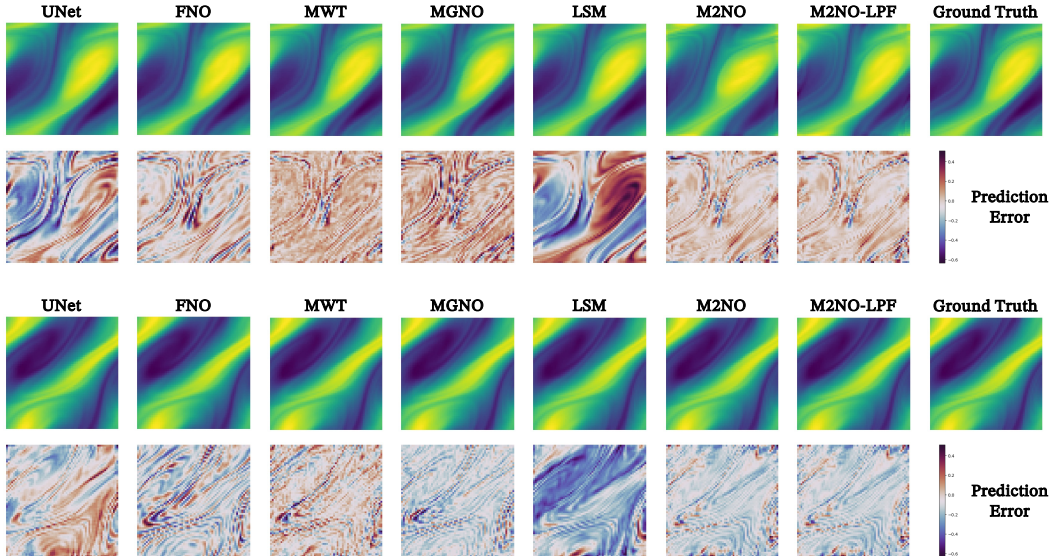


Figure 2: Performance showcases on the Navier-Stokes benchmark, including plots of prediction errors for enhanced clarity.

Benchmarks. To substantiate the superiority of our method, we conducted comprehensive method comparisons across multiple benchmark scenarios [22, 30]. For clearness, we summarize the benchmarks in Table 4 and show the examples of PDEs in Fig 5. More details about PDE benchmarks can be found in Appendix D.

Baselines. We conducted a comprehensive comparison against established methods including UNet [26], Fourier Neural Operator (FNO) [22], Multiwavelet Transform (MWT) [12], Multigrid Neural Operator (MgNO) [15], and Latent Spectral Model (LSM) [33]. It is important to note that MgNO and LSM are specifically tailored for 2D problems.

Implementation. For fairness, all methods were trained over 500 epochs using the L_2 loss function [22], with the ADAM optimizer [18] starting at a learning rate of 10^{-3} and halving every 100 epochs ($\gamma = 0.5$). Batch sizes were set at 512 for 1D PDEs and 16 for 2D PDEs. Unless specified, baselines used default hyperparameters. Experiments were performed on a single Nvidia A800 80GB GPU.

For further details on the baseline models and experimental setup, refer to Appendix F.1.

4.1 Main Results

Table 1 presents a performance comparison across five PDE benchmarks, highlighting M2NO’s superior accuracy. For the 1D benchmarks, M2NO achieves L_2 losses of $2.14\text{E-}06$ for the Advection equation and $7.16\text{E-}06$ for the Burgers equation, demonstrating improvements of 78.41% and 60.49% respectively over the next best model. In the 2D benchmarks, M2NO consistently outperforms other models, achieving the lowest L_2 losses of $9.17\text{E-}04$, $4.07\text{E-}03$ and $1.01\text{E-}01$ for the Navier-Stokes with $\nu = 1e - 3$, $\nu = 1e - 5$ and Diffusion-Reaction equations respectively, marking significant enhancements of 49.75%, 65.77% and 10.15% respectively compared to the next best results. These findings not only underscore the exceptional accuracy of M2NO but also its robust performance across various challenging computational settings.

M2NO’s Superiority in Handling High-Frequency Dynamics. As demonstrated in Fig 2, M2NO excels at mitigating high-frequency errors across various models, particularly within dynamic environments such as the Navier-Stokes benchmark. While the M2NO-LPF variant, equipped with a low-pass filter, outperforms M2NO in time-independent tasks like the Darcy dataset by better maintaining global structures, M2NO consistently surpasses other models in scenarios with rapid, localized changes. This ability to effectively handle high-frequency information underscores M2NO’s advantage in time-dependent datasets, highlighting its suitability for complex, dynamic simulations.

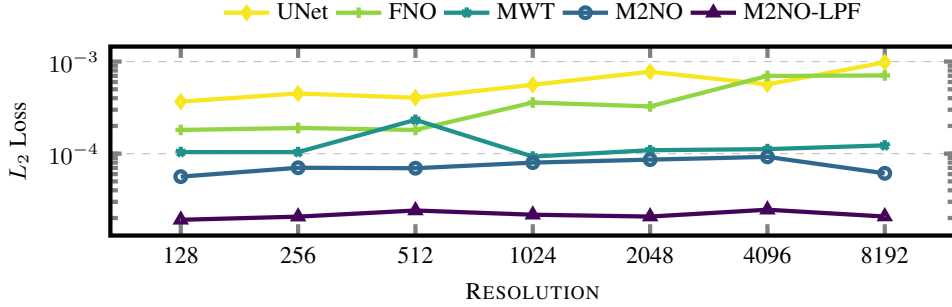


Figure 3: Model performance on the Burgers benchmark at resolutions ranging from 128 to 8192.

Benchmarking M2NO on Complex PDEs. The 2D diffusion-reaction equation is chosen as a benchmark due to its complexity, involving two key variables—the activator and the inhibitor—which are non-linearly coupled. This non-linear coupling presents a significant challenge in accurately modeling the dynamic interactions within the system. Demonstrating its robust modeling capabilities, M2NO secured an improvement exceeding 10% on this challenging benchmark, underscoring its proficiency in handling intricate partial differential equations.

For further experimental results, including outcomes for each PDE under various hyperparameters, please refer to Appendix D. For ablation and hyperparameter study, refer to Appendix E.

4.2 Multiresolution Analysis

Performance under Various Resolutions. As illustrated in Fig. 3, the M2NO model consistently outperforms baseline methods across all tested resolutions in the high-resolution Burgers dataset [22]. This demonstrates its robust capacity to handle the complexities of high-dimensional PDEs without the need for parameter readjustment, even as resolution increases. The M2NO model’s superior performance is further highlighted by its ability to efficiently leverage its multiresolution framework to extract and process information effectively across a wide range of inputs. Detailed results across various datasets and resolutions can be found in Appendix D, offering a comprehensive view of M2NO’s capabilities in diverse computational scenarios.

Table 2: Performance of MWT, M2NO and M2NO-LPF models on the super-resolution task, showing L_2 losses at various resolutions following training at $s = 128$.

Model	$s = 256$	$s = 512$	$s = 1024$	$s = 2048$	$s = 4096$	$s = 8192$
MWT	3.17E-02	3.33E-02	3.38E-02	3.68E-02	3.89E-02	4.56E-02
M2NO	4.81E-03	5.86E-03	6.44E-03	7.70E-03	9.15E-03	1.01E-02
M2NO-LPF	3.25E-03	3.31E-03	2.87E-03	2.76E-03	2.63E-03	2.56E-03

Super-Resolution Performance. Table 2 illustrates the super-resolution capabilities of the MWT, M2NO, and M2NO-LPF models, trained at a base resolution of $s = 128$. This evaluation assesses their ability to upscale to higher resolutions, a critical feature of the M2NO framework that utilizes multiwavelet-based multigrid methods. M2NO-LPF consistently records the lowest L_2 losses across all tested resolutions, demonstrating its superior ability to capture fine details essential for high-resolution tasks. These results highlight the effectiveness of integrating multiwavelet transformations with a multigrid approach in enhancing super-resolution prediction accuracy.

5 Conclusion

We introduced the Multiwavelet-based Algebraic Multigrid Neural Operator (M2NO), a novel framework for solving high-dimensional (referring to the increase in the number of grid points or resolution) partial differential equations using a synergistic blend of multiwavelet transformations and algebraic multigrid techniques. M2NO excels in capturing both global trends and detailed features within PDE solutions, demonstrating superior accuracy and scalability across diverse datasets.

While the Multiwavelet-based Algebraic Multigrid Neural Operator (M2NO) is particularly tailored for complex, time-dependent PDEs with high-frequency and localized changes, this specialization represents a significant advantage, as most practical PDEs exhibit these characteristics. Its current limitation in handling non-uniform grids, which can be adapted through transformations, presents an opportunity for direct integration to further enhance efficiency. Moving forward, efforts will focus on broadening M2NO’s utility across a more diverse range of PDE challenges and simplifying its deployment to maximize its impact in scientific computing.

References

- [1] B. Alpert, G. Beylkin, D. Gines, and L. Vozovoi. Adaptive solution of partial differential equations in multiwavelet bases. *Journal of Computational Physics*, 182(1):149–190, 2002. ISSN 0021-9991. doi: <https://doi.org/10.1006/jcph.2002.7160>. URL <https://www.sciencedirect.com/science/article/pii/S0021999102971603>.
- [2] George Bachman, Lawrence Narici, and Edward Beckenstein. *Fourier and Wavelet Analysis*. Springer New York, NY, 2000.
- [3] A. Boggess and F.J. Narcowich. *A First Course in Wavelets with Fourier Analysis*. Wiley, 2011.
- [4] Achi Brandt. Multi-level adaptive solutions to boundary-value problems. *Mathematics of Computation*, 31(138):333–390, 1977. ISSN 00255718, 10886842. URL <http://www.jstor.org/stable/2006422>.
- [5] William L. Briggs and Van Emden Henson. Wavelets and multigrid. *SIAM J. Sci. Comput.*, 14(2):506–510, 1993.
- [6] W.L. Briggs, V.E. Henson, and S.F. McCormick. *A Multigrid Tutorial, second ed.* SIAM, California, 2000.
- [7] N. M. Bujurke, C. S. Salimath, Ramesh B. Kudenatti, and S. C. Shiralashetti. A fast wavelet-multigrid method to solve elliptic partial differential equations. *Appl. Math. Comput.*, 185(1):667–680, 2007.
- [8] Shuhao Cao. Choose a transformer: Fourier or galerkin. In *NeurIPS*, pages 24924–24940, 2021.
- [9] Ingrid Daubechies. *Ten Lectures on Wavelets*. Society for Industrial and Applied Mathematics, 1992. doi: 10.1137/1.9781611970104. URL <https://epubs.siam.org/doi/abs/10.1137/1.9781611970104>.
- [10] Doreen De Leon. A new wavelet multigrid method. *Journal of Computational and Applied Mathematics*, 220(1):674–685, 2008. ISSN 0377-0427. doi: <https://doi.org/10.1016/j.cam.2007.09.021>. URL <https://www.sciencedirect.com/science/article/pii/S0377042707005080>.
- [11] Engquist and Erding Luo. The multigrid method based on a wavelet transformation and schur complement. In *Semantics Scholar*, 1996.
- [12] Gaurav Gupta, Xiongye Xiao, and Paul Bogdan. Multiwavelet-based operator learning for differential equations. In *NeurIPS*, pages 24048–24062, 2021.
- [13] Morton E. Gurtin. *An Introduction to Continuum Mechanics, Mathematics in Science and Engineering*. Academic Press, Cambridge, 1982.
- [14] Juncai He and Jinchao Xu. Mgnet: A unified framework of multigrid and convolutional neural network. *CoRR*, abs/1901.10415, 2019.
- [15] Juncai He, Xinliang Liu, and Jinchao Xu. Mgno: Efficient parameterization of linear operators via multigrid. *CoRR*, abs/2310.19809, 2023.
- [16] Juncai He, Jinchao Xu, Lian Zhang, and Jianqing Zhu. An interpretive constrained linear model for resnet and mgnet. *Neural Networks*, 162:384–392, 2023.

- [17] Claes Johnson. *Numerical Solution of Partial Differential Equations by the Finite Element Method*. Courier Corporation, North Chelmsford, 2012.
- [18] Diederik P. Kingma and Jimmy Ba. Adam: A method for stochastic optimization. In *ICLR (Poster)*, 2015.
- [19] Gene A. Klaasen and William C. Troy. Stationary wave solutions of a system of reaction-diffusion equations derived from the fitzhugh-nagumo equations. *SIAM Journal on Applied Mathematics*, 44(1):96–110, 1984. ISSN 00361399. URL <http://www.jstor.org/stable/2101307>.
- [20] Nikola B. Kovachki, Zongyi Li, Burigede Liu, Kamyar Azizzadenesheli, Kaushik Bhattacharya, Andrew M. Stuart, and Anima Anandkumar. Neural operator: Learning maps between function spaces with applications to pdes. *J. Mach. Learn. Res.*, 24:89:1–89:97, 2023.
- [21] Zongyi Li, Nikola B. Kovachki, Kamyar Azizzadenesheli, Burigede Liu, Andrew M. Stuart, Kaushik Bhattacharya, and Anima Anandkumar. Multipole graph neural operator for parametric partial differential equations. In *NeurIPS*, 2020.
- [22] Zongyi Li, Nikola Borislavov Kovachki, Kamyar Azizzadenesheli, Burigede Liu, Kaushik Bhattacharya, Andrew M. Stuart, and Anima Anandkumar. Fourier neural operator for parametric partial differential equations. In *ICLR*. OpenReview.net, 2021.
- [23] Lu Lu, Pengzhan Jin, Guofei Pang, Zhongqiang Zhang, and George Em Karniadakis. Learning nonlinear operators via deepnet based on the universal approximation theorem of operators. *Nat. Mach. Intell.*, 3(3):218–229, 2021.
- [24] Ryan McKeown, Rodolfo Ostilla-Mónico, Alain Pumir, Michael P. Brenner, and Shmuel M. Rubinstein. Turbulence generation through an iterative cascade of the elliptical instability. *Science Advances*, 6(9):eaaz2717, 2020. doi: 10.1126/sciadv.aaz2717. URL <https://www.science.org/doi/abs/10.1126/sciadv.aaz2717>.
- [25] M. Raissi, P. Perdikaris, and G.E. Karniadakis. Physics-informed neural networks: A deep learning framework for solving forward and inverse problems involving nonlinear partial differential equations. *Journal of Computational Physics*, 378:686–707, 2019. ISSN 0021-9991. doi: <https://doi.org/10.1016/j.jcp.2018.10.045>. URL <https://www.sciencedirect.com/science/article/pii/S0021999118307125>.
- [26] Olaf Ronneberger, Philipp Fischer, and Thomas Brox. U-net: Convolutional networks for biomedical image segmentation. In *MICCAI (3)*, volume 9351 of *Lecture Notes in Computer Science*, pages 234–241. Springer, 2015.
- [27] T.K. Sarkar, S.P. Magdalena, and C.W. Michael. *Wavelet Applications in Engineering Electromagnetics*. Artech House, Boston, 2002.
- [28] M. F. Shlesinger, B. J. West, and J. Klafter. Lévy dynamics of enhanced diffusion: Application to turbulence. *Phys. Rev. Lett.*, 58:1100–1103, Mar 1987. doi: 10.1103/PhysRevLett.58.1100. URL <https://link.aps.org/doi/10.1103/PhysRevLett.58.1100>.
- [29] K. Stuben. *Algebraic Multigrid (AMG) : An Introduction With Applications*. GMD Forschungszentrum Informationstechnik, 2000.
- [30] Makoto Takamoto, Timothy Praditia, Raphael Leiteritz, Daniel MacKinlay, Francesco Alesiani, Dirk Pflüger, and Mathias Niepert. Pdebench: An extensive benchmark for scientific machine learning. In *NeurIPS*, 2022.
- [31] A. Turing. The chemical basis of morphogenesis. *Bulletin of Mathematical Biology*, 52: 153–197, 1952.
- [32] Abdul-Majid Wazwaz. *Partial Differential Equations: Methods and Applications*. Balkema Publishers, Leiden, 2002.
- [33] Haixu Wu, Tengge Hu, Huakun Luo, Jianmin Wang, and Mingsheng Long. Solving high-dimensional pdes with latent spectral models. In *ICML*, volume 202 of *Proceedings of Machine Learning Research*, pages 37417–37438. PMLR, 2023.

- [34] Jinchao Xu and Ludmil T. Zikatanov. The method of alternating projections and the method of subspace corrections in hilbert space. *Journal of the American Mathematical Society*, 15: 573–597, 2002.
- [35] Jinchao Xu and Ludmil T. Zikatanov. Algebraic multigrid methods. *Acta Numer.*, 26:591–721, 2017.

A Algebraic Multigrid Methods

The key ingredients are the operators I_h^{2h} and I_{2h}^h that change grids:

- A restriction operator I_h^{2h} transfers vectors from the fine grid to the coarse grid
- An interpolation operator I_{2h}^h returns to the fine grid
- The original matrix A_h on the fine grid is approximated by $A_{2h} = I_h^{2h} A_h I$ on the coarse grid.

The spectral radius $\rho(I_h^{2h})$ is called convergence factor. It is roughly the worst factor by which the error is reduced with each relaxation sweep.

A.1 Some Theory

Recall the variational properties:

$$\begin{aligned} A^{2h} &= I_h^{2h} A^h I_{2h}^h \quad (\text{Galerkin property}), \\ I_h^{2h} &= c(I_{2h}^h)^T, \quad c \in I_h^{2h}. \end{aligned} \quad (24)$$

From the orthogonality relationships between the subspaces of a linear operator (Fundamental Theorem of Linear Algebra), we know that

$$\text{Nullspace}(I_h^{2h}) \perp \text{Range}[(I_{2h}^h)^T]. \quad (25)$$

By the second variational property, it then follows that:

$$\text{Nullspace}(I_h^{2h}) \perp \text{Range}(I_{2h}^h), \quad (26)$$

which means that $(\mathbf{q}^h, \mathbf{u}^h) = 0$ whenever $\mathbf{q}^h \in \text{Range}(I_{2h}^h)$ and $I_h^{2h} \mathbf{u}^h = 0$. This is equivalent to the condition that $(\mathbf{q}^h, A^h \mathbf{u}^h) = 0$ whenever $\mathbf{q}^h \in \text{Range}(I_{2h}^h)$ and $I_h^{2h} A^h \mathbf{u}^h = 0$.

This orthogonality property allows the space Ω^h to be decomposed in the form:

$$\Omega^h = \text{Range}(I_{2h}^h) \oplus \text{Nullspace}(I_h^{2h} A^h), \quad (27)$$

which means that if \mathbf{e}^h is a vector in Ω^h , then it may always be expressed as

$$\mathbf{e}^h = \mathbf{s}^h + \mathbf{t}^h, \quad (28)$$

where $\mathbf{s}^h \in \text{Range}(I_{2h}^h)$ and $\mathbf{t}^h \in \text{Nullspace}(I_h^{2h} A^h)$. We associate \mathbf{s}^h with the smooth components of the error and we associate \mathbf{t}^h with the oscillatory components of the error.

B Multiwavelets

B.1 Multiresolution analysis

For $k = 1, 2, \dots$, and $n = 0, 1, 2, \dots$, we define \mathbf{V}_n^k as a space of piecewise polynomial functions,

$$\mathbf{V}_n^k = \{f : \text{the restriction of } f \text{ to the interval } (2^{-n}l, 2^{-n}(l+1)) \text{ is a polynomial of degree less than } k, \text{ for } l = 0, \dots, 2^n - 1, \text{ and } f \text{ vanishes elsewhere}\}. \quad (29)$$

The space \mathbf{V}_n^k has dimension $2^n k$ and

$$\mathbf{V}_0^k \subset \mathbf{V}_1^k \subset \dots \subset \mathbf{V}_n^k \subset \dots \quad (30)$$

Algorithm 1 V-cycle

```

1: procedure VCYCLE( $v^h, f^h$ )
2:   Relax  $\alpha_1$  times on  $A^h u^h = f^h$  with initial guess  $v^h$ 
3:   if  $\Omega^h$  is the coarsest grid then
4:     Relax  $\alpha_2$  times on  $A^h u^h = f^h$  with initial guess  $v^h$ 
5:   else
6:      $r^h \leftarrow f^h - A^h v^h$  ▷ Compute the residual
7:      $f^{2h} \leftarrow I_h^{2h} r^h$  ▷ Restrict the residual to the coarser grid
8:      $v^{2h} \leftarrow 0$  ▷ Initial guess for the coarser grid
9:      $v^{2h} \leftarrow \text{VCYCLE}(v^{2h}, f^{2h})$  ▷ Recursive call
10:     $v^h \leftarrow v^h + I_{2h}^h v^{2h}$  ▷ Prolongate the correction and update
11:    Relax  $\alpha_2$  times on  $A^h u^h = f^h$  with initial guess  $v^h$ 
12:  end if
13: end procedure

```

We define the multiwavelet subspace \mathbf{W}_n^k , $n = 0, 1, 2, \dots$, as the orthogonal complement of \mathbf{V}_n^k in \mathbf{V}_{n+1}^k ,

$$\mathbf{V}_n^k \oplus \mathbf{W}_n^k = \mathbf{V}_{n+1}^k, \quad \mathbf{W}_n^k \perp \mathbf{V}_n^k, \quad (31)$$

and note that \mathbf{W}_n^k is of dimension $2^n k$. Therefore, we have

$$\mathbf{V}_n^k = \mathbf{V}_0^k \oplus \mathbf{W}_0^k \oplus \mathbf{W}_1^k \oplus \dots \oplus \mathbf{W}_{n-1}^k. \quad (32)$$

We define $\mathbf{V}^k = \bigcup_{n=0}^{\infty} \mathbf{V}_n^k$ and observe that \mathbf{V}^k is dense in $L^2([0, 1])$ with respect to norm $\|f\| = \langle f, f \rangle^{1/2}$, where

$$\langle f, g \rangle = \int_0^1 f(x)g(x)dx. \quad (33)$$

Given a basis $\phi_0, \dots, \phi_{k-1}$ of \mathbf{V}_0^k , the space \mathbf{V}_n^k is spanned by $2^n k$ functions which are obtained from $\phi_0, \dots, \phi_{k-1}$ by dilation and translation,

$$\phi_{jl}^n = 2^{n/2} \phi_j(2^n x - l), \quad j = 0, \dots, k-1, \quad l = 0, \dots, 2^n - 1. \quad (34)$$

B.2 Multiwavelets

We introduce piecewise polynomial functions $\psi_0, \dots, \psi_{k-1}$ to be an orthonormal basis for \mathbf{W}_0^k ,

$$\int_0^1 \psi_i(x)\psi_j(x)dx = \delta_{ij}. \quad (35)$$

Since $\mathbf{W}_0^k \perp \mathbf{V}_0^k$, the first k moments of $\psi_0, \dots, \psi_{k-1}$ vanish:

$$\int_0^1 \psi_j(x)x^i dx = 0, \quad i, j = 0, 1, \dots, k-1. \quad (36)$$

The space \mathbf{W}_n^k is spanned by $2^n k$ functions obtained from $\psi_0, \dots, \psi_{k-1}$ by dilation and translation,

$$\psi_{jl}^n(x) = 2^{n/2} \psi_j(2^n x - l), \quad j = 0, \dots, k-1, \quad l = 0, \dots, 2^n - 1, \quad (37)$$

and $\text{supp}(\psi_{jl}^n) = I_{nl}$ denotes the interval $[2^{-n}l, 2^{-n}(l+1)]$. The condition of orthonormality of $\psi_0, \dots, \psi_{k-1}$ yields

$$\int_0^1 \psi_{il}^n(x)\psi_{jm}^{n'}(x)dx = \delta_{ij}\delta_{lm}\delta_{nn'}. \quad (38)$$

The set $\{\phi_0, \dots, \phi_{k-1}\} \cup \{\psi_{jl}^n : j = 0, \dots, k-1, l = 0, \dots, 2^n - 1, n = 0, 1, \dots\}$ therefore forms a complete orthonormal basis for $\mathbb{L}^2([0, 1])$.

B.3 Multiwavelet Transformation

In order to compute projections of functions on subspaces of multiresolution analysis, we consider the two-scale difference equations. In our case, functions ϕ and ψ are known, and we use them to construct the filter coefficients. The relations (30) and (31) between the subspaces may be expressed by the two-scale difference equations,

$$\phi_i(x) = \sqrt{2} \sum_{j=0}^{k-1} (h_{ij}^{(0)} \phi_j(2x) - h_{ij}^{(1)} \phi_j(2x-1)), \quad i = 0, \dots, k-1, \quad (39)$$

$$\psi_i(x) = \sqrt{2} \sum_{j=0}^{k-1} (g_{ij}^{(0)} \phi_j(2x) + g_{ij}^{(1)} \phi_j(2x-1)), \quad i = 0, \dots, k-1, \quad (40)$$

where the coefficients $g_{ij}^{(0)}$, $g_{ij}^{(1)}$ depend on the choice of the order k . The function $\sqrt{2}\phi_0(2x) \dots, \sqrt{2}\phi_{k-1}(2x)$ in (39) are orthonormal on the interval $[0, \frac{1}{2}]$ whereas $\sqrt{2}\phi_0(2x-1) \dots, \sqrt{2}\phi_{k-1}(2x-1)$ are orthonormal on the interval $[\frac{1}{2}, 1]$. The matrices of coefficients

$$H^{(0)} = \{h_{ij}^{(0)}\}, \quad H^{(1)} = \{h_{ij}^{(1)}\}, \quad G^{(0)} = \{g_{ij}^{(0)}\}, \quad G^{(1)} = \{g_{ij}^{(1)}\} \quad (41)$$

are analogs of the quadrature mirror filters. The two-scale equations (39),(40) lead us to a multiresolution decomposition.

By construction, we have $\langle \phi_i, \phi_j \rangle = \delta_{ij}$, $\langle \psi_i, \psi_j \rangle = \delta_{ij}$, and $\langle \phi_i, \phi_j \rangle = 0$ for $i, j = 0, \dots, k-1$, where $\langle \cdot, \cdot \rangle$ is the inner product defined in (33). Using this orthogonality conditions and (39-40), we obtain

$$H^{(0)} H^{(0)T} + H^{(1)} H^{(1)T} = I, \quad (42)$$

$$G^{(0)} G^{(0)T} + G^{(1)} G^{(1)T} = I, \quad (43)$$

$$H^{(0)} G^{(0)T} + H^{(1)} G^{(1)T} = 0. \quad (44)$$

The matrices of coefficients $H^{(0)}$, $H^{(1)}$, $G^{(0)}$, $G^{(1)}$ are analogs of the quadrature mirror filter. We now derive the necessary relations for multiresolution reconstruction. In one dimension, we construct

$$\begin{aligned} H &= \begin{pmatrix} H^{(0)} & H^{(1)} \end{pmatrix} \\ G &= \begin{pmatrix} G^{(0)} & G^{(1)} \end{pmatrix} \end{aligned} \quad (45)$$

to be the operators that transform the basis of the space V_j to the bases of the spaces V_{j+1} and W_{j+1} , respectively. And H and G play the role of separating the low and high frequency components. With the property of $H^{(0)}$, $H^{(1)}$, $G^{(0)}$, $G^{(1)}$, we have

$$\begin{aligned} H^T H + G^T G &= I \\ H G^T &= G H^T = 0 \\ H H^T &= G G^T = I \end{aligned} \quad (46)$$

In two dimensions, the tensor product of one-dimensional multiresolution analyses is used. Analogous to the one-dimensional case, define the operators H and G so that

$$\begin{aligned} H &= H_y \otimes H_x \\ G &= \begin{pmatrix} G_y \otimes H_x \\ H_y \otimes G_x \\ G_y \otimes G_x \end{pmatrix}, \end{aligned} \quad (47)$$

where \otimes is the Kronecker product.

We denote the multiwavelet transform as

$$\mathcal{W} = \begin{pmatrix} H \\ G \end{pmatrix}, \quad (48)$$

Due to the properties of H and G , \mathcal{W} is orthogonal.

B.4 Multiwavelet-based Multigrid method

The following is a brief description of the two-dimensional application of the multiwavelet multigrid method. Given the problem

$$\mathcal{L}_j u = f, \quad (49)$$

where \mathcal{L}_j represents the operator obtained by discretizing a two-dimensional partial differential equation on the fine grid, apply the wavelet transform to both sides of the equation and use the orthogonality of \mathcal{W}_j to obtain

$$(\mathcal{W}_j \mathcal{L}_j \mathcal{W}_j^T) \mathcal{W}_j u = \mathcal{W}_j f. \quad (50)$$

Denote $\tilde{\mathcal{L}}_j = \mathcal{W}_j \mathcal{L}_j \mathcal{W}_j^T$, is partitioned to obtain

$$\tilde{\mathcal{L}}_j = \mathcal{W}_j \mathcal{L}_j \mathcal{W}_j^T = \begin{pmatrix} T_j & B_j \\ C_j & D_j \end{pmatrix}. \quad (51)$$

Using the block UDL decomposition of $\tilde{\mathcal{L}}_j$ and the Schur complement of inverse $\tilde{\mathcal{L}}_j^{-1}$, we can get

$$u = \begin{pmatrix} H^T - G^T D_j^{-1} C_j & G^T \end{pmatrix} \begin{pmatrix} (T_j - B_j D_j^{-1} C_j)^{-1} & 0 \\ 0 & D_j^{-1} \end{pmatrix} \begin{pmatrix} H - B_j D_j^{-1} G \\ G \end{pmatrix} f. \quad (52)$$

Denote the prolongation operator

$$I_{2h}^h = \sqrt{2}(H^T - G^T D_j^{-1} C_j), \quad (53)$$

as well as the restriction operator

$$I_h^{2h} = \frac{1}{\sqrt{2}}(H - B_j D_j^{-1} G). \quad (54)$$

Plugging the prolongation and restriction operators into (15) gives

$$e = I_{2h}^h (T_j - B_j D_j^{-1} C_j)^{-1} I_h^{2h} r + G_j^T D_j^{-1} G_j r. \quad (55)$$

Assuming that $G_j^T D_j^{-1} G_j r$ is small, i.e., r is almost in $\text{Range}(H_j^T)$, the error can be approximated by

$$e = I_{2h}^h (T_j - B_j D_j^{-1} C_j)^{-1} I_h^{2h} r, \quad (56)$$

resulting in

$$(T_j - B_j D_j^{-1} C_j) e_{2h} = I_h^{2h} r_h. \quad (57)$$

By substituting the prolongation operator and restriction operator defined by multiwavelets into the V-cycle Algorithm 1, the Multiwavelet Multigrid method can be obtained.

C Proof of Theorem 1

The proof relies on several key assumptions and properties of the operators involved:

1. **Assumptions on Subspace Solvers:** We assume that the subspace solvers T_i satisfy the following conditions:
 - $R(T_i) = V_i$ and $T_i : V_i \rightarrow V_i$ is isomorphic for each i .
 - Each factor $I - T_i$ is nonexpansive, i.e., $\|I - T_i\| \leq 1$, which is equivalent to $(T_i v, T_i v) \leq 2(T_i v, v)$ for all $v \in V$.
2. **Symmetrization of Operators:** The symmetrized operator is given by $\bar{T}_i = T_i + T_i^* - T_i^* T_i$. This operator is nonnegative on V and symmetric positive definite on V_i .
3. **Main Result:** Under the above assumptions, we establish that:

$$\|E\|_{L(V,V)} \leq \left(1 + \sup_{\|v\|=1} \inf_{\sum_{i=1}^J v_i = v} \sum_{i=1}^J (\bar{T}_i^{-1} T_i^* w_i, T_i^* w_i) \right)^{-1}. \quad (58)$$

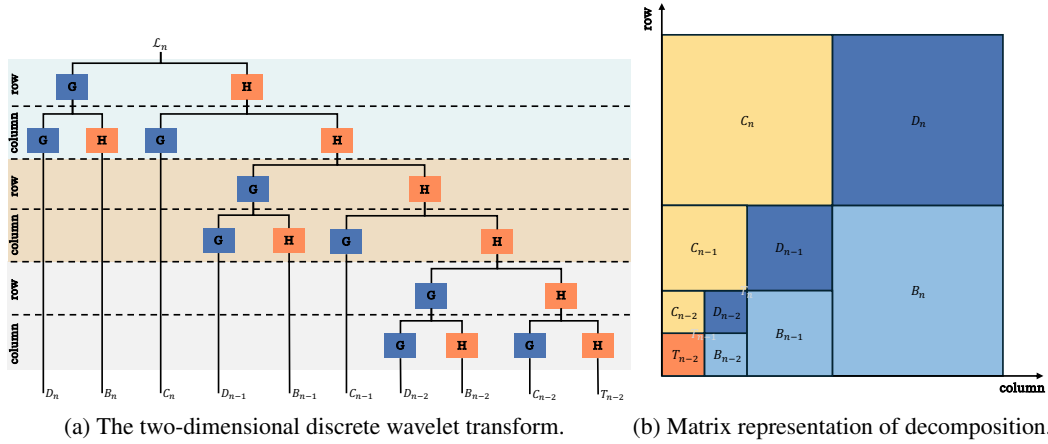


Figure 4: (a) Two-dimensional discrete wavelet transform with G (high-pass) and H (low-pass) filters. Horizontal lines represent frequency bands; vertical lines show decomposition levels. (b) Matrix representation of decomposition, dividing L_n into submatrices B_n , C_n , and D_n .

Table 3: Definitions of Symbols.

Symbol	Description
\mathcal{L}_{mg}	V-cycle multigrid operator
A	Elliptic operator
$*$	Convolution operator
$\ \cdot\ _A$	Energy norm defined as $\ u\ _A^2 = (u, A * u)_{L^2(\Omega)}$
c	A constant unaffected by the discretization parameter h
Ω	Domain of the problem
T_i	Subspace solvers
V_i	Subspaces
I	Identity operator
\bar{T}_i	Symmetrized operator $\bar{T}_i = T_i + T_i^* - T_i^* T_i$
L_n	Elliptic operator associated with the Green's function
w_i	Intermediate vectors defined by $w_i = \sum_{j=i}^J v_j - T_i^{-1} v_i$
$\lambda_{\min}(T_i)$	Smallest eigenvalue of T_i

To complete the proof, we need to show that the constant c_0 in the main result is finite. This involves demonstrating that the series involving T_i and \bar{T}_i is bounded. The definitions of symbols are summarized in Table. 3.

First, we need to show that the constant c_0 is finite. We define c_0 as follows:

$$c_0 = \sup_{\|v\|=1} \inf_{\sum v_i=v} \sum_{i=1}^J (\bar{T}_i^{-1} T_i^* w_i, T_i^* w_i), \quad (59)$$

where $w_i = \sum_{j=i}^J v_j - T_i^{-1} v_i$.

Using the properties of the symmetrized operator \bar{T}_i and the nonexpansive property of T_i , we have:

$$(T_i v, T_i v) \leq 2(T_i v, v) \leq 2\|T_i v\| \|v\| \leq 2\|T_i\| \|v\|^2. \quad (60)$$

Since \bar{T}_i is symmetric positive definite on V_i , we have:

$$(\bar{T}_i v, v) \geq \lambda_{\min}(\bar{T}_i) \|v\|^2, \quad (61)$$

where $\lambda_{\min}(\bar{T}_i)$ is the smallest eigenvalue of \bar{T}_i .

We now show that the series involving T_i and \bar{T}_i is bounded:

$$\sum_{i=1}^J (\bar{T}_i^{-1} T_i^* w_i, T_i^* w_i) \leq \sum_{i=1}^J \frac{1}{\lambda_{\min}(\bar{T}_i)} (T_i^* w_i, T_i^* w_i). \quad (62)$$

Since $\|T_i\| \leq 1$ and $\|T_i^*\| \leq 1$, we have:

$$(T_i^* w_i, T_i^* w_i) \leq \|T_i^*\|^2 \|w_i\|^2 \leq \|w_i\|^2. \quad (63)$$

Therefore,

$$\sum_{i=1}^J (\bar{T}_i^{-1} T_i^* w_i, T_i^* w_i) \leq \sum_{i=1}^J \frac{1}{\lambda_{\min}(\bar{T}_i)} \|w_i\|^2. \quad (64)$$

We need to show that $\|w_i\|$ is bounded. By the definition of w_i , we have:

$$w_i = \sum_{j=i}^J v_j - T_i^{-1} v_i. \quad (65)$$

Using the fact that T_i^{-1} is bounded, we get:

$$\|w_i\| \leq \left\| \sum_{j=i}^J v_j \right\| + \|T_i^{-1}\| \|v_i\| \leq \sum_{j=i}^J \|v_j\| + \|T_i^{-1}\| \|v_i\|. \quad (66)$$

Since $\|v\| = 1$ and $v = \sum_{i=1}^J v_i$, we have:

$$\|v\|^2 = \left\| \sum_{i=1}^J v_i \right\|^2 \leq J \sum_{i=1}^J \|v_i\|^2 \leq J. \quad (67)$$

Thus,

$$\|w_i\| \leq \sum_{j=i}^J \|v_j\| + \|T_i^{-1}\| \|v_i\| \leq J + \|T_i^{-1}\|. \quad (68)$$

Combining the above results, we get:

$$\sum_{i=1}^J (\bar{T}_i^{-1} T_i^* w_i, T_i^* w_i) \leq \sum_{i=1}^J \frac{1}{\lambda_{\min}(\bar{T}_i)} (J + \|T_i^{-1}\|)^2. \quad (69)$$

Since $\lambda_{\min}(\bar{T}_i)$ and $\|T_i^{-1}\|$ are finite, the constant c_0 is finite.

Finally, combining these results, we have:

$$\|u - \mathcal{L}_{mg}(A * u)\|_A \leq \left(1 - \frac{1}{c}\right) \|u\|_A, \quad (70)$$

where c is the aforementioned constant.

Thus, the operator \mathcal{L}_{mg} demonstrates uniform convergence with the desired properties.

D Details for Benchmarks and Additional Experiments

We detail the benchmark configurations in Table 4 and illustrate PDE examples in Figure 5. Below, we outline the generation process for each category of governing PDEs and present comprehensive experimental results for each benchmark, exploring variations across different coefficients and resolutions.

For the Navier-Stokes benchmark, we utilize the dataset released by [22], available for download at this URL with MIT License. For other benchmarks, we employ widely recognized PDEs from the PDE benchmark suite, a popular resource frequently used in contemporary methods. These benchmarks can be accessed at this URL under the CC BY 4.0 License.

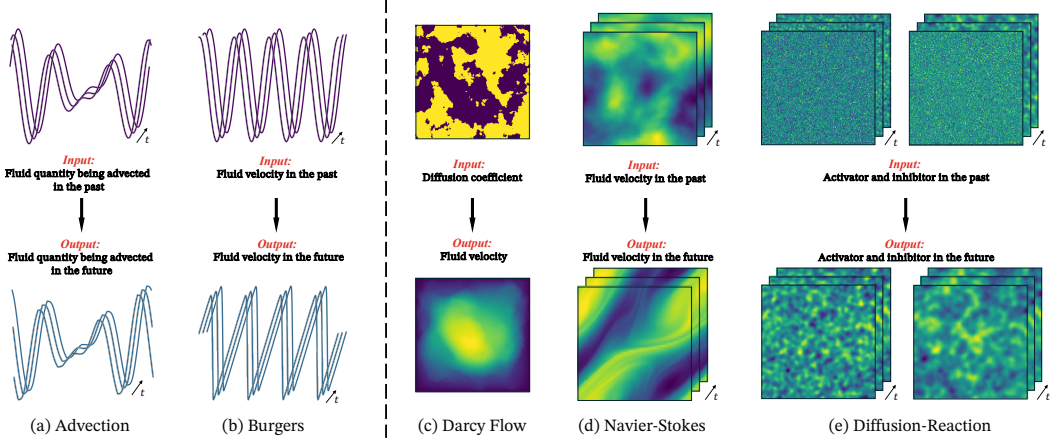


Figure 5: **Examples of PDE benchmarks across different scenarios.** Left side (1D): (a) Advection, where input and output represent the fluid quantity being advected at different times; (b) Burgers, showcasing the evolution of fluid velocity. Right side (2D): (c) Darcy Flow, depicting changes in fluid velocity influenced by diffusion coefficients; (d) Navier-Stokes, illustrating fluid velocity variations over time; (e) Diffusion-Reaction, visualizing the interaction dynamics of activators and inhibitors.

Table 4: Summary of benchmarks. Each benchmark varies by dimension, time dependency, boundary conditions, and resolution. Specific parameters include the viscosity (ν) values for the Burgers benchmarks, set at $\{0.001, 0.01, 0.1, 1.0\}$, and diffusion coefficients (β) for the Advection benchmark, set at $\{0.1, 1.0, 4.0\}$.

Benchmark	# Dimension	Time dependent	Boundary condition	Spatial resolution	Temporal resolution
Burgers	1D	Yes	Periodic	1024	200
Burgers-HR	1D	Yes	Periodic	8192	-
Advection	1D	Yes	Periodic	1024	200
Darcy Flow	2D	No	Dirichlet	512*512	-
Navier Stokes	2D	Yes	Periodic	64*64	20
Diffusion-Reactiong	2D	Yes	Periodic	128*128	100

D.1 1D Advection Equation

The advection equation [30] models pure advection behavior without non-linearity. Its expression is given as:

$$\frac{\partial u(t, x)}{\partial t} + \beta \frac{\partial u(t, x)}{\partial x} = 0, \quad x \in (0, 1), t \in (0, 2], \quad (71)$$

$$u(0, x) = u_0(x), \quad x \in (0, 1),$$

where β is a constant advection speed.

As the initial condition, we use a superposition of sinusoidal waves:

$$u_0(x) = \sum_{k_i=k_1}^{k_N} A_i \sin(k_i x + \phi_i), \quad (72)$$

where $k_i = \frac{2\pi n_i}{L_x}$ are wave numbers with n_i being integers randomly selected in $[1, n_{\max}]$, A_i are random float numbers uniformly chosen in $[0, 1]$, and ϕ_i are phases randomly chosen in $(0, 2\pi)$. We set $k_{\max} = 8$ and $N = 2$.

The exact solution of the system is given by:

$$u(t, x) = u_0(x - \beta t). \quad (73)$$

In our dataset, we consider only periodic boundary conditions.

Results. Table 5 highlights the M2NO model's superior performance in solving the 1D Advection equation across various diffusion coefficients (β) and resolutions (s). M2NO consistently outperforms

Table 5: Benchmarks on 1D Advection equation at various β and input resolution s .

Model	beta=0.1				beta=1.0				beta=4.0			
	s=128	s=256	s=512	s=1024	s=128	s=256	s=512	s=1024	s=128	s=256	s=512	s=1024
U-net	3.32E-05	2.42E-05	3.21E-05	2.94E-05	3.05E-05	1.54E-05	3.52E-05	3.52E-05	3.79E-05	2.59E-05	4.32E-05	3.44E-05
FNO	1.11E-05	5.79E-06	4.58E-06	6.27E-06	2.19E-05	2.16E-05	2.74E-05	2.17E-05	2.09E-05	2.10E-05	1.70E-05	1.68E-05
MGNO	/	/	/	/	/	/	/	/	/	/	/	/
MWT Leg	8.74E-06	3.44E-06	8.55E-06	8.14E-06	3.12E-06	4.06E-06	4.30E-06	4.41E-06	3.50E-06	6.55E-06	9.89E-06	9.91E-06
LSM	/	/	/	/	/	/	/	/	/	/	/	/
M2NO-schur	9.40E-07	8.20E-07	5.90E-07	5.50E-07	1.40E-06	1.01E-06	1.01E-06	1.06E-06	1.41E-06	2.19E-06	2.34E-06	2.14E-06
M2NO-LPF	1.12E-06	8.80E-07	8.60E-07	6.20E-07	1.45E-06	1.00E-06	1.11E-06	1.51E-06	1.44E-06	2.49E-06	2.77E-06	2.35E-06
Promotion	89.24%	76.16%	87.12%	91.23%	55.13%	75.37%	76.51%	75.96%	59.71%	66.56%	76.34%	78.41%

traditional models like U-net and FNO, particularly at higher β values, which suggest increased diffusivity. Notably, M2NO-LPF performs well at lower resolutions, indicating its effectiveness in capturing essential features with limited data. These results demonstrate M2NO’s robust adaptability to different physical and computational conditions, reinforcing its potential for complex PDE challenges.

D.2 1D Burgers’ Equation

The Burgers’ equation [30, 22, 12] is a PDE that models non-linear behavior and diffusion processes in fluid dynamics. It is expressed as:

$$\begin{aligned} \frac{\partial u}{\partial t} &= -u \frac{\partial u}{\partial x} + \nu \frac{\partial^2 u}{\partial x^2}, \quad x \in (0, 1), t \in (0, 2], \\ u(0, x) &= u_0(x), \quad x \in (0, 1), \end{aligned} \quad (74)$$

where ν is the diffusion coefficient, which is assumed to be constant in our dataset.

Table 6: Benchmarks on 1D Burgers equation at various ν and input resolution s .

Model	nu=1.0				nu=0.1				nu=0.01				nu=0.001			
	s=128	s=256	s=512	s=1024												
U-net	8.27E-05	4.78E-05	3.16E-05	6.10E-05	4.33E-05	4.26E-05	4.56E-05	3.74E-05	5.30E-05	4.98E-05	2.59E-05	4.99E-05	8.29E-05	6.66E-05	6.04E-05	3.83E-05
FNO	9.18E-06	1.15E-05	2.71E-05	3.14E-05	8.00E-06	8.40E-06	8.70E-06	8.06E-06	1.70E-05	1.21E-05	1.10E-05	1.10E-05	4.65E-05	3.48E-05	2.28E-05	1.81E-05
MGNO	/	/	/	/	/	/	/	/	/	/	/	/	/	/	/	/
MWT Leg	3.46E-06	4.66E-06	5.27E-06	6.49E-06	3.84E-06	3.48E-06	3.48E-06	3.63E-06	1.81E-05	1.17E-05	1.15E-05	1.18E-05	5.24E-05	3.69E-05	2.50E-05	2.07E-05
LSM	/	/	/	/	/	/	/	/	/	/	/	/	/	/	/	/
M2NO-schur	1.64E-06	1.51E-06	2.36E-06	3.45E-06	8.30E-07	1.22E-06	1.58E-06	1.86E-06	3.32E-06	3.29E-06	2.78E-06	3.58E-06	2.24E-05	1.01E-05	1.09E-05	7.16E-06
M2NO-LPF	1.56E-06	2.08E-06	2.44E-06	2.66E-06	8.40E-07	1.35E-06	1.65E-06	1.83E-06	3.18E-06	3.32E-06	3.27E-06	3.83E-06	2.30E-05	9.36E-06	9.50E-06	7.52E-06
Promotion	54.91%	67.60%	55.22%	59.01%	78.39%	64.94%	54.60%	49.59%	81.24%	71.95%	74.77%	67.40%	51.96%	73.07%	58.26%	60.49%

Results. Table 6 showcases the performance of models on the 1D Burgers equation across different viscosities (ν) and resolutions (s). The M2NO model consistently demonstrates low L_2 losses, particularly excelling at higher viscosities where the equation dynamics are less complex. Conversely, at lower viscosities, characterized by greater nonlinearity, the M2NO-LPF variant proves more effective, especially at finer resolutions, underscoring its superior handling of more challenging dynamic conditions. This illustrates the robustness of both M2NO variants in adapting to diverse computational demands and physical scenarios.

D.3 2D Darcy Flow

Darcy flow [12, 30] is a fundamental relationship in hydrogeology, describing the flow of a fluid through a porous medium. We experiment on the steady-state of the 2D Darcy flow equation on the unit box, where it takes the following form:

$$\begin{aligned} \nabla \cdot (a(x)\nabla u(x)) &= f(x), \quad x \in (0, 1)^2, \\ u(x) &= 0, \quad x \in \partial(0, 1)^2, \end{aligned} \quad (75)$$

where $a(x)$ is the permeability field, $u(x)$ is the hydraulic head, and $f(x)$ is the source term.

Results. Table 7 delineates the performance benchmarks on the Darcy Flow equation across varying input resolutions (s). Notably, both M2NO and M2NO-LPF exhibit competitive L_2 loss metrics, particularly excelling at lower resolutions. While M2NO maintains strong performance consistently

across the range, M2NO-LPF demonstrates exceptional results at $s = 512$, with an L_2 loss of 9.64E-03, suggesting enhanced efficiency in capturing flow characteristics at higher resolutions. These findings indicate the effectiveness of the M2NO models in accurately modeling fluid flow through porous media, which is central to the simulation of Darcy Flow.

Table 7: Benchmarks on Darcy Flow equation at various input resolution s .

Model	s=32	s=64	s=128	s=256	s=512
Unet	8.43E-02	6.18E-02	5.71E-02	6.10E-02	9.25E-02
FNO	5.55E-02	4.27E-02	5.44E-02	3.24E-02	2.17E-02
MGNO	5.12E-02	2.97E-02	2.84E-02	4.12E-02	4.10E-02
MWT Leg	4.44E-02	2.27E-02	2.59E-02	2.63E-02	3.68E-02
M2NO	4.17E-02	4.75E-02	4.85E-02	5.83E-02	2.73E-02
M2NO-LPF	4.20E-02	3.66E-02	2.46E-02	2.88E-02	9.64E-03

D.4 2D Diffusion-Reaction Equation

We consider a two-dimensional diffusion-reaction type PDE that combines a diffusion process with a rapid evolution from a source term [30]. The equation is written as:

$$\partial_t u = D_u \partial_{xx} u + D_u \partial_{yy} u + R_u, \quad \partial_t v = D_v \partial_{xx} v + D_v \partial_{yy} v + R_v, \quad (76)$$

where D_u and D_v are the diffusion coefficients for the activator and inhibitor, respectively, and $R_u = R_u(u, v)$ and $R_v = R_v(u, v)$ are the reaction functions for the activator and inhibitor, respectively.

The reaction functions are defined by the FitzHugh-Nagumo equation [19], written as:

$$\begin{aligned} R_u(u, v) &= u - u^3 - k - v, \\ R_v(u, v) &= u - v, \end{aligned} \quad (77)$$

where $k = 5 \times 10^{-3}$, and the diffusion coefficients for the activator and inhibitor are $D_u = 1 \times 10^{-3}$ and $D_v = 5 \times 10^{-3}$, respectively. The initial condition is generated as standard normal random noise $u(0, x, y) \sim \mathcal{N}(0, 1.0)$ for $x \in (-1, 1)$ and $y \in (-1, 1)$.

We include the 2D diffusion-reaction equation as an example because it serves as a challenging benchmark problem. It involves two variables of interest, the activator and inhibitor, which are non-linearly coupled. Additionally, it has real-world applicability, particularly in modeling biological pattern formation [31, 30].

Table 8: Benchmarks on Diffusion-Reaction equation at various input resolution s .

Model	$s = 32$	$s = 64$	$s = 128$
Unet	2.18E-01	1.64E-01	1.46E-01
FNO	2.00E-01	1.56E-01	1.64E-01
MGNO	2.03E-01	1.50E-01	1.12E-01
MWT Leg	2.20E-01	1.51E-01	1.15E-01
LSM	2.92E-01	2.02E-01	1.58E-01
M2NO	1.97E-01	1.42E-01	1.01E-01
M2NO-LPF	1.99E-01	1.44E-01	1.06E-01
Promotion	1.60%	5.34%	10.15%

Results. Table 8 displays the performance benchmarks on the 2D Diffusion-Reaction equation, a complex model that simulates biological pattern formation involving non-linearly coupled variables—activator and inhibitor. Across various input resolutions (s), the M2NO models, particularly M2NO and M2NO-LPF, demonstrate improved performance compared to traditional methods such as U-net, FNO, and others. Notably, the M2NO model achieves the lowest L_2 losses at higher resolutions ($s = 128$), indicating a 10.15% improvement in accuracy, reflecting its capability to more effectively handle the intricate dynamics of this challenging benchmark. The M2NO-LPF variant also shows significant performance enhancements, particularly at medium resolutions ($s = 64$), suggesting its adeptness in capturing essential features of the diffusion-reaction processes.

D.5 Navier-Stokes Equation

Navier-Stokes equations describe the motion of viscous fluid substances [22, 12, 15], and are used to model ocean currents, weather, and air flow. We experiment on the 2D Navier-Stokes equation for a viscous, incompressible fluid in vorticity form on the unit torus, which takes the following form:

$$\begin{aligned} \frac{\partial w(x, t)}{\partial t} + u(x, t) \cdot \nabla w(x, t) - \nu \Delta w(x, t) &= f(x), & x \in (0, 1)^2, & t \in (0, T], \\ \nabla \cdot u(x, t) &= 0, & x \in (0, 1)^2, & t \in [0, T], \\ w_0(x) &= w(x, t = 0), & x \in (0, 1)^2, & \end{aligned} \quad (78)$$

where $w(x, t)$ is the vorticity, $u(x, t)$ is the velocity field, ν is the kinematic viscosity, and $f(x)$ is a forcing function.

Table 9: Benchmarks on Navier-Stoke equation at various ν , T and N .

Model	$\nu=1e-3$	$\nu=1e-4$	$\nu=1e-5$
	T=50 N=1000	T=30 N=10000	T=20 N=1000
UNet	3.86E-03	1.38E-02	2.15E-02
FNO-2D	4.95E-03	9.56E-03	1.72E-02
MGNO	3.39E-03	6.58E-03	1.27E-02
MWT-2D-Leg	1.83E-03	3.83E-03	1.19E-02
LSM	6.00E-03	1.02E-02	1.71E-02
M2NO	9.17E-04	1.59E-03	4.07E-03
M2NO-LPF	1.04E-03	2.01E-03	7.69E-03
Promotion	49.75%	58.47%	65.77%

Results. Table 9 displays the performance of various models on the Navier-Stokes equation across different viscosities, temporal resolutions, and grid sizes. The Multiwavelet-based Algebraic Multigrid Neural Operator (M2NO) consistently outperforms other models such as UNet, FNO-2D, and LSM. M2NO achieves its lowest L_2 error of 9.17×10^{-4} under conditions of $\nu = 1 \times 10^{-3}$, $T = 50$, and $N = 1000$. This superior accuracy is maintained even under more challenging conditions; for instance, at $\nu = 1 \times 10^{-4}$ with $T = 30$ and $N = 10000$, it registers an L_2 error of 1.59×10^{-3} , and at the finest tested viscosity of $\nu = 1 \times 10^{-5}$, $T = 20$, and $N = 1000$, the error is 4.07×10^{-3} . M2NO not only shows remarkable stability and performance efficiency across these diverse settings but also demonstrates significant improvements in model accuracy, with promotion rates of 49.75%, 58.47%, and 65.77% across the various test conditions.

E Ablation and Hyperparameter Study

The ablation study uses Burgers' equation with $\nu = 1e - 3$ under the resolution of 1024 as a reference example. The baseline M2NO is configured with levels [1, 1, 1, 2, 2, 3], $k = 8$, $c = 8$, Schur-based operators and comprises 5 architectural layers. We conduct the ablation and hyperparameters study by changing one model configuration and fixing the others.

Table 10: Ablation results comparing the L_2 error of different M2NO configurations. The removal of multilevel and multiwavelet features, along with a variant using a low-pass filter (M2NO-LPF), are evaluated against the baseline model.

Model Configuration	L_2 Error
w/o multilevel	4.53E-05
w/o multiwavelet	4.56E-05
M2NO-LPF	7.52E-06
M2NO (Baseline)	7.16E-06

Ablation Study Analysis. In our ablation study of the Multiwavelet-based Algebraic Multigrid Neural Operator (M2NO) on Burgers' equation with $\nu = 1e - 3$ and a resolution of 1024, summarized

in Table 10, we investigated the impact of different model configurations on L_2 error. The baseline M2NO, utilizing full multilevel and multiwavelet features, achieved an L_2 error of $7.16\text{E-}06$. Removal of the multilevel component or the multiwavelet feature resulted in similar increases in error to $4.53\text{E-}05$ and $4.56\text{E-}05$, respectively, underscoring their critical roles in reducing error. The M2NO-LPF variant, employing a low-pass filter instead of a traditional multigrid operator, demonstrated a slight increase in error to $7.52\text{E-}06$, suggesting that while LPF simplifies the model, it retains much of the baseline’s efficacy, particularly in smoothing high-frequency details. These findings highlight the essential contributions of multilevel and multiwavelet components to the M2NO framework and suggest the potential for simpler models in specific scenarios.

Table 11: Hyperparameter study results for the M2NO model, detailing the L_2 error across various configurations. Changes in grid level, wavelet number, basis number, and layer number are evaluated against the baseline to assess their impact on model performance.

Hyperparameter Type	Model Configuration	L_2 Error
Iteration	[1,1,1,1,1,1]	$7.35\text{E-}06$
Grid Level	[1,2,3]	$6.45\text{E-}06$
Wavelet Number	c=2	$1.83\text{E-}05$
	c=4	$8.16\text{E-}06$
	c=6	$6.20\text{E-}06$
	c=16	$5.29\text{E-}06$
Basis Number	k=2	$1.28\text{E-}05$
	k=4	$7.15\text{E-}06$
Layer Number	layer=3	$8.24\text{E-}06$
	layer=4	$7.19\text{E-}06$
	layer=6	$4.66\text{E-}06$
Baseline	M2NO	$7.16\text{E-}06$

Hyperparameter Study Analysis. The hyperparameter study of M2NO, presented in Table 11, explored the impact of various model configurations on the L_2 error. Adjustments were made across multiple parameters, including iteration steps, grid levels, wavelet numbers, basis numbers, and the number of layers. Notably, increasing the grid levels from a flat [1,1,1,1,1,1] to a varied [1,2,3] configuration reduced the L_2 error from $7.35\text{E-}06$ to $6.45\text{E-}06$. Changes in the wavelet number revealed that using $c=16$ minimized the error to $5.29\text{E-}06$, indicating a more significant wavelet count enhances accuracy. Similarly, an optimal layer count was identified, with six layers achieving the lowest error at $4.66\text{E-}06$. Conversely, varying the basis number showed that a higher count does not always correlate with lower error, as $k=4$ performed better than $k=2$. These results illustrate the nuanced impacts of each parameter on model performance, guiding further refinement and optimization of M2NO configurations for enhanced precision in scientific simulations.

F Implementation Details

F.1 Baseline and Benchmark Construction

Time-dependent tasks. In our benchmarks, all tasks are time-dependent, except for Darcy Flow. These tasks are auto-regressive, requiring sequential predictions for each subsequent time step. Accordingly, we employ the 2D versions of the Multiwavelet-based Algebraic Multigrid Neural Operator (M2NO), along with the Fourier Neural Operator (FNO) and Multiwavelet Transform (MWT) models, to predict the next time frame in a step-by-step manner across all benchmarks.

Data splits. For the Diffusion-Reaction and Navier-Stokes (NS) datasets, the data is allocated with 80% used for training, 10% for validation, and 10% for testing. For all other datasets, the split is 60% for training, 20% for validation, and 20% for testing.

Baselines. We implemented all baseline models using their official source code and corresponding default parameters. However, for the LSM model, the default patch size of [4, 4] was not suitable for a resolution of 32×32 . Consequently, we adjusted the patch size to [2, 2] to ensure compatibility. For fairness in comparison, all methods were trained over 500 epochs using the L_2 loss function [22]

and the ADAM optimizer [18] with an initial learning rate of 10^{-3} , which was halved every 100 epochs ($\gamma = 0.5$). Batch sizes were set at 512 for 1D PDEs and 16 for 2D PDEs. All experiments were conducted on a single Nvidia A800 80GB GPU.

F.2 Model Architecture

In the Multiwavelet-based Multigrid Neural Operator (M2NO), the neural networks A , S , B , C and D^{-1} are implemented as single-layer convolutional neural networks (CNNs). The orthonormal polynomial (OP) basis utilized is the Legendre (Leg) basis, chosen with both uniform and non-uniform measures μ_0 , in alignment with the Multiwavelet Transform (MWT)[12] methodologies.

From a computational perspective, the *restriction* and *prolongation* operators depicted in (16) and Fig 1 specifically target the transformation of multiscale and multiwavelet coefficients. Despite this focus on coefficients, the actual input and output of the model are point-wise function samples, specifically (a_i, u_i) . To address this, we synthesize the data sequence into conceptual functions $f_a = \sum_{i=1}^N a_i \phi_{ji}^n$ and $f_u = \sum_{i=1}^N u_i \phi_{ji}^n$, positing them within the space V_n^k where $n = \log_2 N$. It is critical to note that these functions, f_a and f_u , are employed primarily for theoretical articulation and not for direct computation, serving as a notational convention rather than functional entities in the model’s operations.

Generalizing Dimensionality According to Discrete Wavelet Transform (DWT) theory, the dimension of the analyzed matrix must be a power of 2 [27]. Within the Algebraic Multigrid (AMG) context, such a restriction could severely limit the method’s applicability. Consequently, we generalize as follows: the dimension of the restriction operator I_h^{2h} , for all k , is defined to be $(N/2) \times N$ where

$$N = \begin{cases} n, & \text{if } n \text{ is even,} \\ n + 1, & \text{if } n \text{ is odd,} \end{cases} \quad (79)$$

with $n = \dim(A_j)$. If n is odd, the dimensions of the matrix and the corresponding right-hand side vector are incremented by one.

F.3 Model Configurations

The primary configurations for the Multiwavelet-based Multigrid Neural Operator (M2NO) are detailed in Table 12, and those for the M2NO with Low-Pass Filter (M2NO-LPF) in Table 13. Except where specifically noted, model parameters remain consistent across different hyperparameters and resolutions within the same benchmark.

Table 12: Model Configurations of M2NO.

Modules	Advection	Burgers	Navier-Stokes	Darcy	Diffusion-Reaction
num_layer	5	5	5	5	5
c	8	8	2	1	4
k	8	8	8	4	4
grid_levels	[1,1,2,2,2,3,3]	[1,1,1,2,2,2,3]	[1,1,2,2,2,3]	[3,3,2,2,1]	[2,2,1,1,1]
padding_mode	'circular'	'circular'	'zeros'	'zeros'	'zeros'
bias	TRUE	TRUE	TRUE	TRUE	TRUE
base	'legendre'	'legendre'	'legendre'	'legendre'	'legendre'
initializer	'xavier_normal'	'xavier_normal'	'xavier_normal'	'xavier_normal'	'xavier_normal'
norm	TRUE	TRUE	TRUE	TRUE	TRUE
operator	'schur'	'schur'	'schur'	'schur'	'schur'
activation	'gelu'	'gelu'	'gelu'	'gelu'	'gelu'

Table 13: Model Configurations of M2NO-LPF.

Modules	Advection	Burgers	Navier-Stokes-1e-3	Navier-Stokes-1e-4	Navier-Stokes-1e-5	Darcy	Diffusion-Reaction
num_layer	5	5	5	5	5	5	4
c	8	8	1	1	2	2	1
k	8	8	8	8	8	4	8
grid_levels	[1,1,1,2,2,2,3]	[1,1,1,2,2,2,3]	[1,1,2,2,2,3]	[1,1,2,2,2,3]	[1,1,2,2,2,3]	[3,3,2,2,1]	[3,3,2,2,2]
padding_mode	'circular'	'circular'	'circular'	'circular'	'circular'	'circular'	'circular'
bias	TRUE	TRUE	TRUE	TRUE	TRUE	TRUE	TRUE
base	'legendre'	'legendre'	'legendre'	'legendre'	'legendre'	'legendre'	'legendre'
initializer	'xavier_normal'	'xavier_normal'	'xavier_normal'	'xavier_normal'	'xavier_normal'	'xavier_normal'	'xavier_normal'
norm	TRUE	TRUE	TRUE	TRUE	TRUE	TRUE	TRUE
operator	'lpf'	'lpf'	'lpf'	'lpf'	'lpf'	'lpf'	'lpf'
activation	'gelu'	'gelu'	'gelu'	'gelu'	'gelu'	'gelu'	'gelu'